Downloaded from orbit.dtu.dk on: Apr 30, 2024

DTU Library

Gate-tunable Thermoelectric Effect in Oxide Thin Films at Room Temperature

Chatterjee, Arindom; Lobato, Carlos Nunez; Rosendal, Victor; Anhøj, Thomas Aarøe; Grivel, Jean Claude; Trier, Felix; Christensen, Dennis Valbjørn; Pryds, Nini

Published in:
Advanced Electronic Materials

Link to article, DOI:
10.1002/aelm.202300683

Publication date:
2024

Document Version
Publisher's PDF, also known as Version of record

Link back to DTU Orbit

Citation (APA):
Chatterjee, A., Lobato, C. N., Rosendal, V., Anhøj, T. A., Grivel, J. C., Trier, F., Christensen, D. V., & Pryds, N. (2024). Gate-tunable Thermoelectric Effect in Oxide Thin Films at Room Temperature. *Advanced Electronic Materials*, *10*(3), Article 2300683. https://doi.org/10.1002/aelm.202300683

General rights
Copyright and moral rights for the publications made accessible in the public portal are retained by the authors and/or other copyright owners and it is a condition of accessing publications that users recognise and abide by the legal requirements associated with these rights.

- Users may download and print one copy of any publication from the public portal for the purpose of private study or research.
- You may not further distribute the material or use it for any profit-making activity or commercial gain
- You may freely distribute the URL identifying the publication in the public portal

If you believe that this document breaches copyright please contact us providing details, and we will remove access to the work immediately and investigate your claim.

ADVANCED ELECTRONIC MATERIALS Open Access
www.advelectronicmat.de

Check for updates

Gate-tunable Thermoelectric Effect in Oxide Thin Films at Room Temperature

*Arindom Chatterjee, Carlos Nunez Lobato, Victor Rosendal, Thomas Aarøe Anhøj, Jean-Claude Grivel, Felix Trier, Dennis Valbjørn Christensen, and Nini Pryds**

Over the past several decades, major efforts have been directed toward the optimization of carrier concentrations to maximize thermoelectric performance. Chemical doping is an effective way to control carriers, but electrostatic gating provides a continuous tuning knob that enables effective and dynamic changes to the carrier density. Here, a method is reported that uses an electric-double-layer (EDL) transistor-based ionic liquids gating to adjust the thermoelectric properties of thin films made from Nb-doped $SrTiO_3$ (Nb-STO). This technique allows us to effectively change these properties at room temperature by varying the concentration of charge carriers within a broad range. A combination of lower film thickness and intrinsic carrier concentration leads to an enhanced ionic liquid-gated response, resulting in an 18-fold enhancement in power factor at room temperature for a 14 nm thin 4% Nb-STO film at gate voltages within ±3.0 V. The present study offers new insights and strategies toward enhanced gate tunable thermoelectric properties in thin films.

1. Introduction

Thermoelectric generators (TEGs) convert waste heat into electricity through the Seebeck effect. TEGs are noiseless, require no maintenance, and are highly reliable with no moving parts and a long lifespan. TEGs can generate sufficient energy output for powering low-power electronic devices with small footprint sizes (<1 cm^2), which makes them one of the attractive on-board powering devices for internet-of-thing (IoT) applications.[1-3] Here, thin film-based thermoelectric research is very important in the context of the miniaturization of the devices.[4–9]

A. Chatterjee, C. N. Lobato, V. Rosendal, T. A. Anhøj, J.-C. Grivel, F. Trier, D. V. Christensen, N. Pryds
Department of Energy Conversion and Storage
DTU Nanolab
Technical University of Denmark
Lyngby, Kongens 2800, Denmark
E-mail: nipr@dtu.dk

The ORCID identification number(s) for the author(s) of this article can be found under https://doi.org/10.1002/aelm.202300683

© 2023 The Authors. Advanced Electronic Materials published by Wiley-VCH GmbH. This is an open access article under the terms of the Creative Commons Attribution License, which permits use, distribution and reproduction in any medium, provided the original work is properly cited.

DOI: 10.1002/aelm.202300683

The dimensionless figure-of-merit, zT, is a parameter that defines the thermoelectric conversion efficiency and is desirable to be as high as possible. The zT is defined as $zT = (\sigma S^2/\kappa)T$, where S, σ, κ, and T denote the Seebeck coefficient, electrical conductivity, thermal conductivity, and temperature, respectively. One of the challenging objectives of thermoelectric research is to optimize zT by balancing and optimizing these parameters simultaneously through the charge carriers in the material. A proper balance between the Seebeck coefficient and the electrical conductivity controls the maximum power factor (σS^2), while the balance between the power factor and thermal conductivity determines the figure of merit.[10,11]

Electrostatic gating is potentially an ideal method for voltage-controlled tuning of a wide range of carrier concentrations. Efficient charge depletion and accumulation can be accomplished by employing gate insulators with high dielectric constants. Conventional dielectrics such as SiO_2, HfO_2, and $SrTiO_3$ can generate capacitance in the order of ≈10 nF cm^{-2}, which generally can modulate charge carriers within the range of 10^{11} – 10^{13} cm^{-2}.[12] This approach has been used to improve the thermoelectric power factor of SiGe nanowires by applying negative gate voltages across SiO_2 dielectric.[13] However, in some cases, the maximum tunable limit of carriers by conventional gate dielectrics is limited by the dielectric breakdown of the gate. This is the case for Nb doped-$SrTiO_3$ (Nb-STO), an n-type material often used as a thermoelectric material, where the high sheet carrier densities of the materials do not allow significant changes of charge carriers with conventional dielectric gate.[14]

By using chemical doping, the power factor for 5–100% Nb-doped $SrTiO_3$ thin films was tuned between 0.4-to-2.6 mW m^{-1} K^{-2} by varying the carrier densities between 10^{21} and 10^{22} cm^{-3}.[8] This corresponds to a sheet carrier density between 10^{15}–10^{16} cm^{-2} for 100 nm thin films,[8] which makes it impractical to tune the carrier density with conventional electrostatic gating. In contrast, ionic liquid gating provides an alternative way to tune materials with high carrier densities.[15] The use of electric-double-layer (EDLT) enables the exertion of a substantial electric field at the junction between liquid and solid which leads to pronounced depletion of the carrier density at the solid side. Certain liquid electrolytes, like 1-ethyl-3-methylimidazolium-bis (trifluoro

sulfonyl) amide, known as EMIM-TFSI,[16,17] can generate large capacitances as high as ≈10 – 50 μF cm^{-2}[2]. This allows the electrolytes to either deplete or accumulate charge carriers in the order of 10^{15} cm^{-2}.[18] Ionic-gating has proven to be an effective way to tune the thermoelectric properties with, for example, liquid ionic-gating applied on black phosphorus crystal showing a steep increase in thermopower from a value of ≈150 to ≈550 μV K^{-1} due to gate-voltage-driven strong depletion of the conducting channel.[19] Ionic liquid gating on the same material system, also showed that tuning both the carrier density and the mobility is possible without affecting the Seebeck coefficient significantly.[19] Similarly, a high power factor of 50 μW cm^{-1} K^{-2} was obtained by ionic-liquid gating at the surface of a ZnO single crystal.[20] Ionic liquid gating on $SrTiO_3$ single crystal surfaces also shows remarkable tuning abilities, which results in an insulator to a metal transition,[21] an insulator to a superconductor transition,[22] nonlinear transport in $SrTiO_3$ nanowires,[23] tunable Kondo scattering at lower temperatures,[24] and modulations of the thermoelectric power.[25,26] However, so far, the gate tunability of the thermoelectric power factor of doped-$SrTiO_3$ thin films has not been exploited at temperatures relevant to thermoelectric energy harvesting.

In this paper, we report the tunability of the thermoelectric power factor of Nb-STO films at room temperature by ionic liquid gating. The tunability of the charge carrier concentration and, therefore the transport properties, were carried out for a set of two different Nb-STO films with variable film thicknesses grown on $(LaAlO_3)_{0.3}(Sr_2AlTaO_6)_{0.7}$ (100) substrates (LSAT (100)). We found that a combination of lower Nb-doping and reduced film thicknesses leads to an enhanced tunability of the ion-gated thermoelectric power factor, resulting in an 18-fold enhancement.

2. Results and Discussions

Two sets of Nb-doped $SrTiO_3$ thin films with variable film thicknesses were synthesized on LSAT (100) single crystal substrates: the first set is 6% Nb-doped $SrTiO_3$ (i.e., $SrTi_{0.94}Nb_{0.06}O_3$) films, and the second set of films is 4% Nb-doped $SrTiO_3$ (i.e., $SrTi_{0.96}Nb_{0.04}O_3$).

We choose LSAT (100) substrates for three different reasons: i) Growth of Nb-STO films on $SrTiO_3$ (100) substrates may generate conductive interfaces, while growth on LSAT substrates ensures that there is no interfacial conductance at the interface between the LSAT substrate and the Nb-STO films,[27] ii) the lattice mismatch between the Nb-STO and the LSAT is small (≈ −1%) resulting in good epitaxial growth of films with only slight compressive strain[28]; and iii) thermal conductivity of LSAT substrate is lower than $SrTiO_3$ (100) or $LaAlO_3$ (100), and hence, relatively larger temperature gradients can be generated for thermoelectric measurements.[29]

Figure 1a depicts a schematic illustration of the ionic liquid-gated device structure. In this setup, we conducted gate-tunable measurements of the electronic conductivity, Hall coefficients, and thermopower of Nb-STO conducting channels. A real image of the photoresist-patterned device is shown in Figure 1b prior to the metal evaporation process on our chips. Hall bar patterning of Nb-STO films was done by making use of amorphous La-doped $CaMnO_3$ thin films ($La_xCa_{1-x}MnO_3$, x = 0.1) as hard mask[30] and necessary metal electrodes were evaporated for thermoelectric transport coefficients measurements by electron-beam metal evaporation technique. Experimental details of the device patterning and transport measurements are documented in Figures S1–S4 of Supporting Information.

An example of the evaluation of the temperature differences (ΔT) and thermoelectric voltages ($\Delta V_{Seebeck}$) obtained between two thermometers (Th1 and Th2 in Figure 1a) as a function of heater current (I_{Heater}) is depicted in Figure 1c. These measurements were performed at 300 K. A range of currents from −14 to 14 mA was applied to the resistive heater, resulting in a maximum ΔT = 1.25 K on the LSAT substrate. Both quantities (ΔT and $\Delta V_{Seebeck}$) show parabolic behavior at both positive- and negative heater currents due to the quadratic dependence of the Joule heating on the current. The linear dependence between ΔT and $\Delta V_{Seebeck}$ is a signature of thermoelectric effects, resulting in a Seebeck coefficient of −165.2 μV K^{-1}. Information on thermometer calibrations and the measurements of ΔT as well as $\Delta V_{Seebeck}$ can be found in the Supporting Information.

Figure 2a depicts high-resolution X-ray diffraction patterns of ≈37 nm thin 6% and 4% Nb-STO films. It shows clear appearances of film reflections between 42 to 50 degrees in 2θ along with the high intensity (002) substrate reflections, as indicated by arrows. The appearance of the Keissig fringes on both sides of (002) film reflections assures high-quality interfaces between the film and the substrate. We found that the (002) film reflections of 4% Nb-STO film are slightly shifted towards the right at a 2θ angle. This indicates a decrease of the c-parameter on decreasing the concentration of the Nb doping in STO film lattice. The c-parameters for the 6% and 4% doped films are determined to be ≈3.948 and 3.920 Å, respectively. The decrease in c-parameters with reduced Nb doping is due to Nb having a larger atomic radius than Ti therefore, replacing Ti in the STO lattice expands the unit cell according to Vegard's law.[33] The X-ray reflectivity measurements of film thicknesses for the two Nb-doped samples are displayed in Figure 2b.

Figure 2c,d displays the effects of thickness and doping on electronic conductivity, and sheet carrier density (and carrier mobility in Figure S5b, Supporting Information), all measured at room temperature. The highest values were measured for 37 nm 6% Nb-STO films with a conductivity of ≈445 S cm^{-1}, a sheet carrier density of ≈4.6 × 10^{15} $cm^{-2,}$ and a mobility of ≈2.2 cm^2 V^{-1} s^{-1}. As the film thickness reduces from 37 nm to ≈14 nm, the conductivity drops continuously from 445 to 83 S cm^{-1}, as shown by the black squares in Figure 2c. Films thinner than 10 nm (specifically at 6 and 4 nm) have resistances so high that they surpass our equipment's measurement capabilities. The decrease in conductivity is associated with a decrease in both the carrier concentration and mobility (Figure S5, Supporting Information). For the 6% Nb-STO films with thicknesses ranging from 37 to 14 nm, the carrier concentration steadily drops from ≈4.6 × 10^{15} to 9.1 × 10^{14} cm^{-2}. Within the same thickness range, the carrier mobility also declines from 2.5 to 0.75 cm^2 V^{-1} s^{-1}. Similar trends are found for the 4% Nb-STO films but with an overall lower conductivity and sheet carrier density.

Figure 3a shows the electronic resistance of films with different film thicknesses and gate voltages as a function of time. Measurements were taken at room temperature at a range of voltages of $-1.0V \leq V_{LG} \leq +1.0$ V in vacuum. To estimate the electronic conductivity or resistivity, we make two assumptions: 1) The film's

© 2023 The Authors. Advanced Electronic Materials published by Wiley-VCH GmbH

2199160x, 2024, 3, Downloaded from https://onlinelibrary.wiley.com/doi/10.1002/aelm.202300683 by Danish Technical Knowledge, Wiley Online Library on [21/03/2024]. See the Terms and Conditions (https://onlinelibrary.wiley.com/terms-and-conditions) on Wiley Online Library for rules of use; OA articles are governed by the applicable Creative Commons License

ADVANCED ELECTRONIC MATERIALS
Open Access
www.advelectronicmat.de

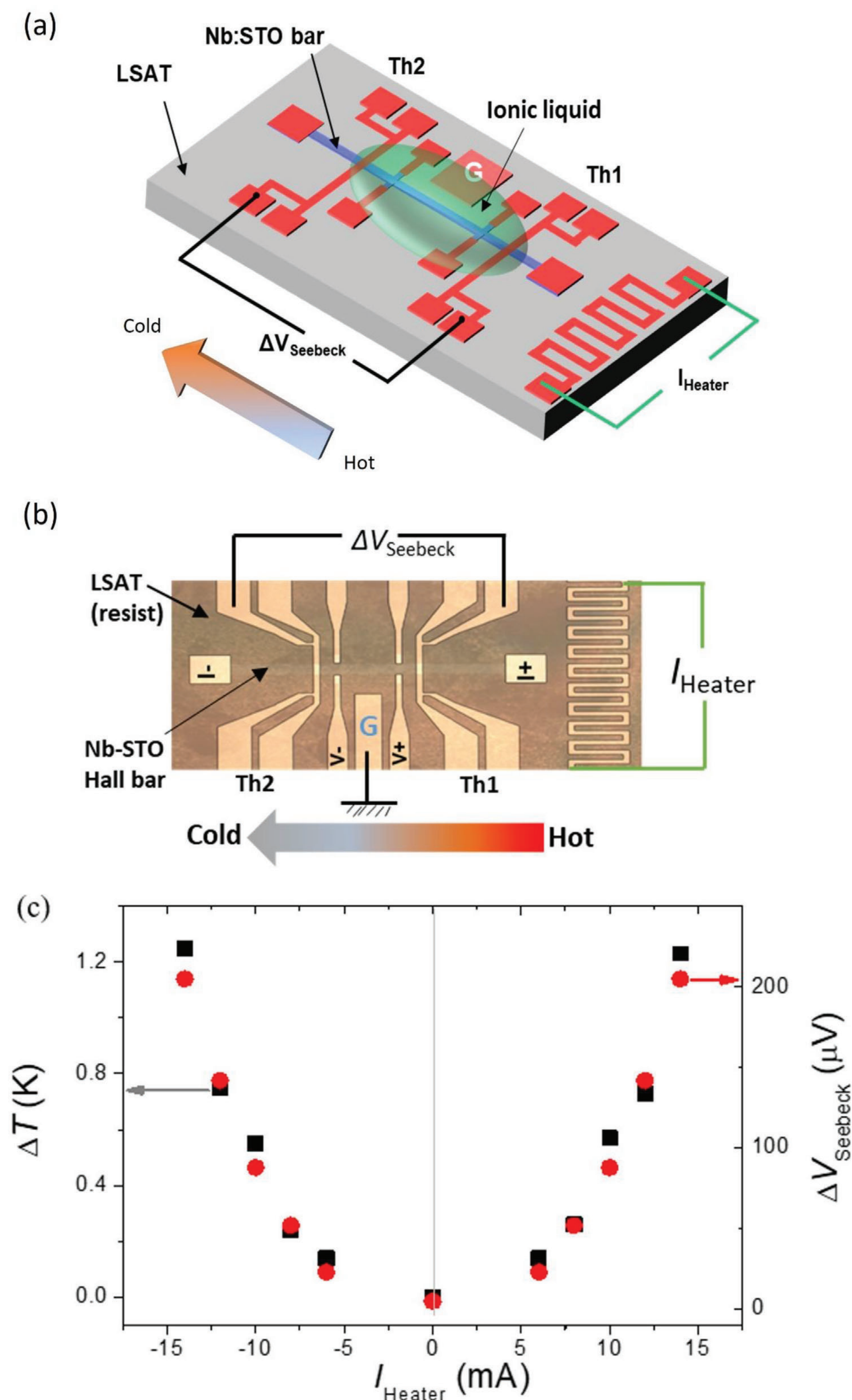

Figure 1. Gate tunable thermoelectric properties. a) Schematic illustration of the ionic liquid-gated thermoelectric device, b) a real image of the photoresist-patterned device, and c) an example of temperature differences (ΔT) and thermoelectric voltages ($\Delta V_{Seebeck}$) produced as a function of heater current in the device.

© 2023 The Authors. Advanced Electronic Materials published by Wiley-VCH GmbH

2199160x, 2024, 3, Downloaded from https://onlinelibrary.wiley.com/doi/10.1002/aelm.202300683 by Danish Technical Knowledge, Wiley Online Library on [21/03/2024]. See the Terms and Conditions (https://onlinelibrary.wiley.com/terms-and-conditions) on Wiley Online Library for rules of use; OA articles are governed by the applicable Creative Commons License

2199160x, 2024, 3, Downloaded from https://onlinelibrary.wiley.com/doi/10.1002/aelm.202300683 by Danish Technical Knowledge, Wiley Online Library on [21/03/2024]. See the Terms and Conditions (https://onlinelibrary.wiley.com/terms-and-conditions) on Wiley Online Library for rules of use; OA articles are governed by the applicable Creative Commons License

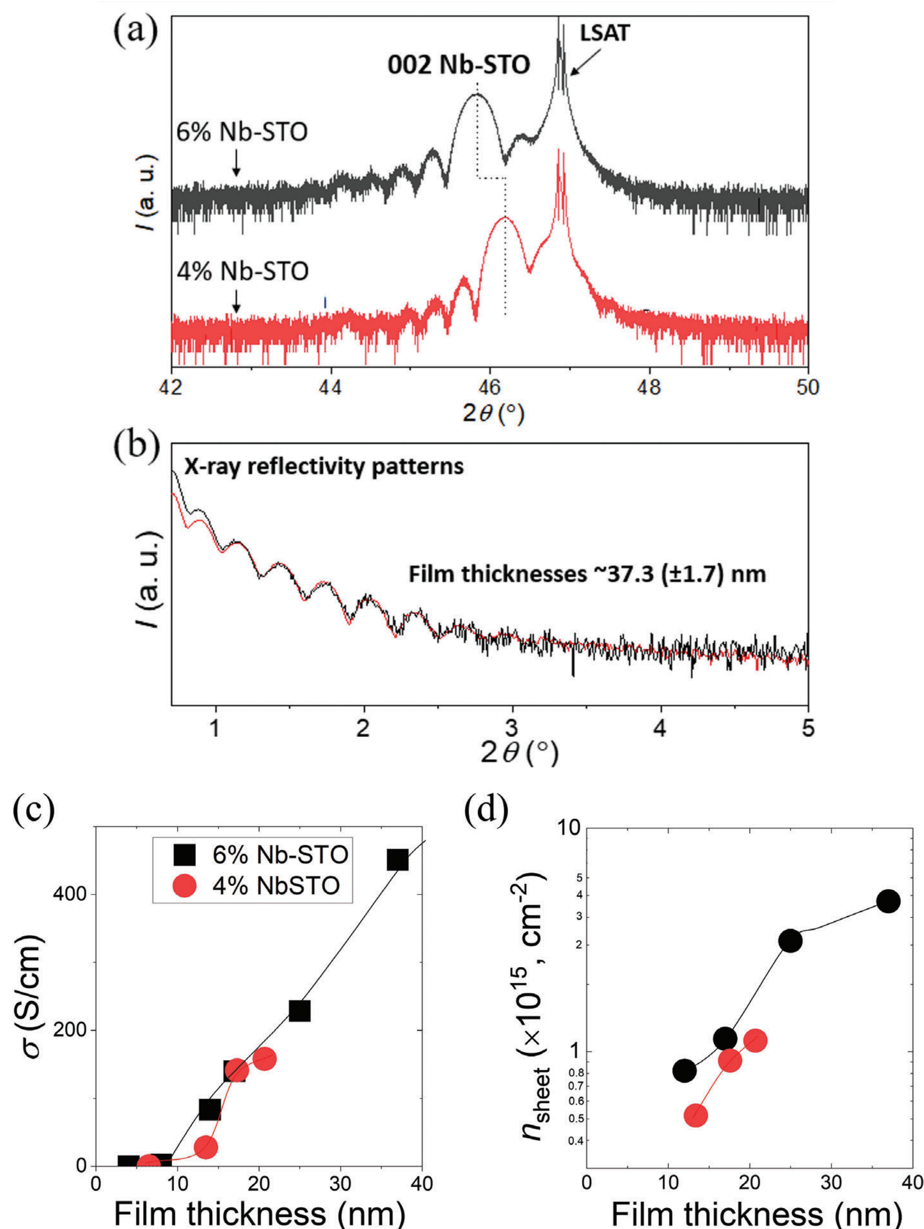

Figure 2. Structural and electronic properties. a) Standard X-ray diffraction patterns, and b) X-ray reflectivity patterns of ≈37 nm thick of 4%- and 6% Nb-doped $SrTiO_3$ films. c) and d) are thickness and doping concentration dependent on electronic conductivity and carrier concentration, respectively.

volume remains unchanged when gate voltages are applied and 2) Electron depletion or accumulation does not affect the entire volume of the film. We used a fixed current source of 1×10^{-6} A between the source and the drain contact for measuring the resistance as a function of liquid gating. Within the voltage range of $-1.0 \leq V_{LG} \leq +1.0$ V, the leakage current through the gate was < 1 nA. The electronic resistance of the 37 nm film drops instantly from its initial value to a lower value when a small positive voltage of $V_{LG} = +0.3$ V is applied to the gate. The decrease in resistance when applying positive gate voltage confirms the *n*-type conductivity in our Nb-STO film, which is consistent with the sign of the Hall coefficients. The resistance turns back to its initial value when the gate voltage is turned off, showing the reversibility of this process. When a small negative gate voltage of $V_{LG} = -0.3$ V is applied to the gate, the resistance increases and then drops non-hysteretically when the voltage is turned off. We observed a similar behavior at higher gate voltages. All cycles were fully reversible within the $-1.0 \leq V_{LG} \leq +1.0$ V range, and the changes in resistance scaled with the magnitude of the applied gate voltage. For the 37 nm film, we observed a resistance change of ≈7–8% within ±1.0 V. Similar trends were noted for the 17 and 14 nm films. However, thinner films exhibited a more pronounced ion-gated response compared to the thicker ones. As gate voltages are adjusted to ±3.0 V, resistance either increases or decreases. It is important to note that at gate voltages beyond ±4 V, the reproducibility of the process tends to diminish. We want to highlight

 © 2023 The Authors. Advanced Electronic Materials published by Wiley-VCH GmbH

ADVANCED ELECTRONIC MATERIALS
Open Access
www.advelectronicmat.de

2199160x, 2024, 3, Downloaded from https://onlinelibrary.wiley.com/doi/10.1002/aelm.202300683 by Danish Technical Knowledge, Wiley Online Library on [21/03/2024]. See the Terms and Conditions (https://onlinelibrary.wiley.com/terms-and-conditions) on Wiley Online Library for rules of use; OA articles are governed by the applicable Creative Commons License

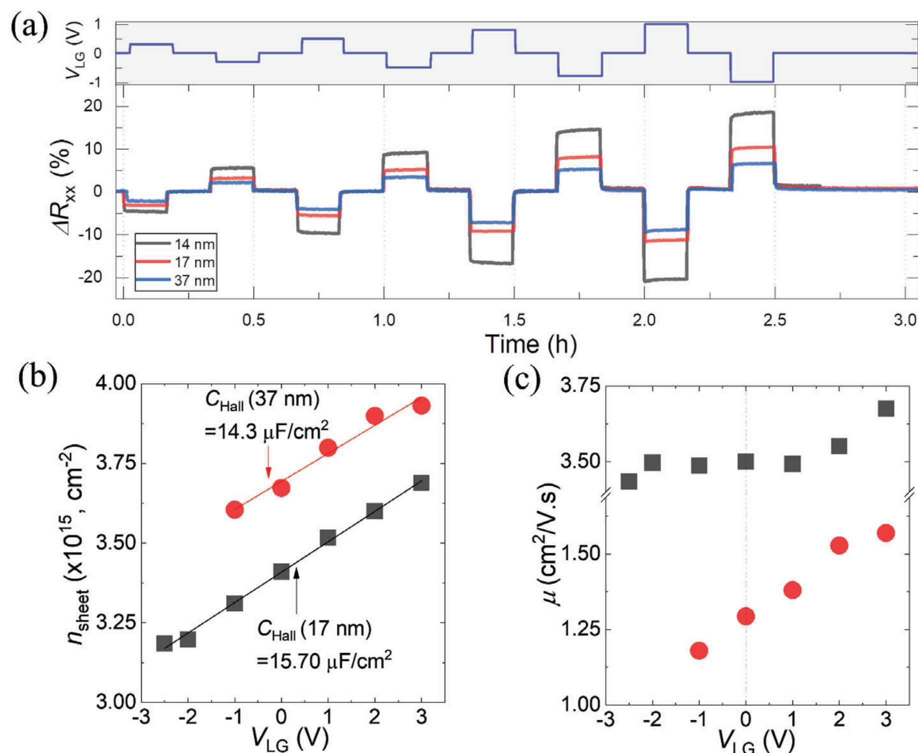

Figure 3. Gate-tunable electronic transport properties. a) Kinetics of the gate voltage- and film thickness-dependent electronic resistance for 6% Nb-STO films at room temperature. b) Hall effect measurements at 200 K. Gate voltage dependence on the sheet carrier's concentration. c) Carrier's mobility for 17 and 37 nm thick 6% Nb-doped $SrTiO_3$ films, respectively.

that there was no chemical interaction detected between the liquid used for gating and the film in our experiments.

The variation in electronic resistance when using ionic liquid gating could be linked to changes in carrier concentration, mobility, or both. To address this, we performed ionic liquid-gated Hall measurements at 200 K. We conducted Hall measurements below the ionic liquid freezing point (≈235 K) to minimize ion thermal fluctuations and ensure a static electric field with pA-level leakage current. Samples were heated to 250 K for ionic liquid polarization using gate voltages, then cooled to 200 K for precise Hall assessments. Figure 3b compares the tunability of sheet carrier concentrations for 37 and 17 nm 6% Nb-STO films. The density of sheet carriers increases linearly from 3.2×10^{15} to 3.7×10^{15} cm^{-2} for the 17 nm thick film when gate voltage varies from −3.0 to +3.0 V with no sign of saturation. For the 37 nm film, the carrier density increases from 3.6×10^{15} to 3.9×10^{15} cm^{-2} within the range of $-1.0 \leq V_{LG} \leq +3.0$ V.

Figure 3c displays the mobility of the 37 nm and 17 nm films as a function of gate voltage. Interestingly, the carrier mobility for both films shows a continuous increase as the gate voltage increases from −2.0 V to +3.0 V for the 37 nm film whereas the effect is somewhat nonlinear for the 17 nm film, yet still monotonously increasing with the gate. The mobility as a function of gate voltage is steeper for the 37 nm film than the 17 nm one. These results indicate that the mobility contributes significantly to the conductivity of the thicker film compared to the thinner film. Indeed, our results show that for the 37 nm film, the increase in mobility with the gate is more pronounced than the rise in carrier concentration. It is worth noting that films with thicknesses ≤ 6 nm could not be gated by ionic liquid but remained insulating probably due to the so-called dead layers (see Figure S5 in Supporting Information). Overall, we find that both carrier concentration and mobility boost the electronic resistance/conductance.

The Hall capacitance (C_{Hall}) was also calculated from the slope of the sheet carrier density versus gate voltage curves as shown in Figure 3b, resulting in a similar Hall capacitance of C_{Hall} = 15.7±0.6 μF cm^{-2} for the 17 nm thick film compared to C_{Hall} = 14.3±0.8 μF cm^{-2} for the 37 nm film. Film thickness has a subtle influence on Hall capacitance. The capacitance of other EMIM-TFSI-gated structures measured by impedance spectroscopy show values in the range of 20–35 μF cm^{-2} at room temperature,[15,16] which is in reasonable agreement with our Hall capacitance measurements.

We studied the gate tunability of the thermoelectric power factor in the 6% and 4% Nb-STO films, focusing on the 14 nm thickness since these films exhibited the most pronounced gate response. **Figure 4a,b** shows how the electronic conductivity and thermopower at room temperature are influenced by gate voltage and doping. In the absence of any gate voltages, the 6% Nb-STO film shows a conductivity of ≈53 S cm^{-1}, and a Seebeck coefficient of ≈ −165 μV K^{-1} with a carrier density ≈9.1×10^{14} cm^{-2}, while the 4% Nb-STO film shows a conductivity of 23 S cm^{-1}, a Seebeck coefficient of −292 μV K^{-1}, and a carrier density 5.1×10^{14} cm^{-2}. The increase in the conductivity and simultaneous decrease in the thermopower for higher doping levels is a

© 2023 The Authors. Advanced Electronic Materials published by Wiley-VCH GmbH

2199160x, 2024, 3, Downloaded from https://onlinelibrary.wiley.com/doi/10.1002/aelm.202300683 by Danish Technical Knowledge, Wiley Online Library on [21/03/2024]. See the Terms and Conditions (https://onlinelibrary.wiley.com/terms-and-conditions) on Wiley Online Library for rules of use; OA articles are governed by the applicable Creative Commons License

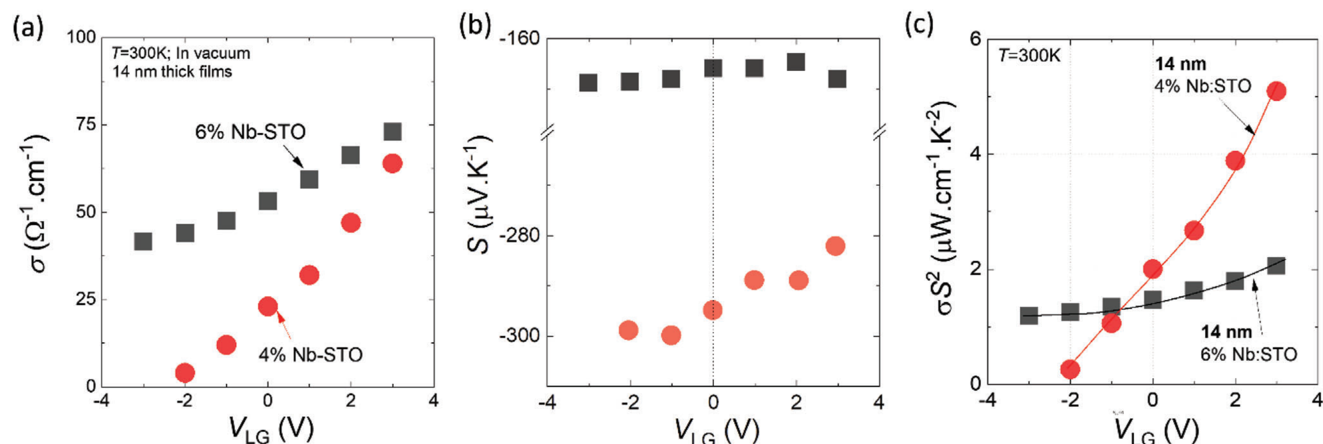

Figure 4. Gate-tunable a) Electronic transport- b) thermopower, and c) power factor of 14 nm thick 4%- and 6% Nb-doped $SrTiO_3$ films at room temperature.

consequence of the increased sheet carrier density, since the conductivity is proportional to the carrier concentration, while thermopower has an inversely proportional relationship to the carrier concentration.

The conductivity is found to increase continuously from ≈40 to ≈74 S cm^{-1} when the gate voltage sweeps from −3.0 to +3.0 V for the 6% Nb-STO film, as shown in Figure 4a. Interestingly, the thermopower continuously increases from −169 to −164 μV K^{-1} with increasing the gate voltage (see Figures S6 and S7, Supporting Information for the enlarged data version).

Similarly, the conductivity increases rapidly from ≈4 to 64 S cm^{-1} for the 4% Nb-STO film when gate voltage sweeps from −2.0 to +3.0 V. On the other hand, the thermopower increases almost linearly from −300 to −282 μV K^{-1} within the same range of gate voltages. For the 4% Nb-STO film, the response of the conductivity and the thermopower to the gate are much more pronounced than the 6% Nb-doped films.

The thermoelectric power factor as a function of gate voltage is presented in Figure 4c. At room temperature with zero gate voltage, the power factor is ≈ 1.46 μW cm^{-1} K^{-2} for the 14 nm thick 6% Nb-STO film and ≈ 1.98 μW cm^{-1} K^{-2} for the 14 nm 4% Nb-STO film. The power factor for the 6% Nb-STO film can be adjusted by the gate voltage, changing by a factor of 1.7, from ≈1.18 to 2.06 μW cm^{-1} K^{-2}, as gate voltages are swept from −3.0 to +3.0 V. In contrast, the power factor for 4% Nb-STO film is tuned continuously from 0.26 to 5.09 μW cm^{-1} K^{-2} by sweeping gate voltages from −2.0 to +3.0 V, resulting in an 18.5 times increase. The effect of applying gate voltage on the thermoelectric power factor is significantly higher for 4%-Nb-STO film than for the 6% Nb-STO film. Overall, the combination of lower film thickness and lower Nb-doping concentrations leads to a much higher enhancement in the ionic liquid to tune the thermoelectric power factor. Oxygen migration induced by ionic gating is a plausible mechanism that could impact the thermoelectric properties, and this possibility cannot be disregarded in our current study. Investigating this mechanism further could be a valuable direction for future research.

To investigate the role of carrier mobility on the electrical conductivity and thermopower, Hall effect measurements were carried out as a function of gate voltages (between 0 to 3 V) for 14 nm thick 4% Nb-STO. Figures S9 and S10 (Supporting Information) summarize the data. Within the same gate voltage range, carrier concentration rises steadily from 4.9×10^{14} to 7.7×10^{14} cm^{-2} (a 1.57-fold increase), while electron mobility nearly doubles from 0.41 to 0.75. This enhanced mobility elevates the electrical conductivity without impacting the Seebeck coefficient, leading to a sharp rise in the power factor. Using ionic liquid gating to tune mobility in thermoelectric thin films offers advantages in performance not achievable with traditional chemical doping.

To analyze the Seebeck coefficient's variation with gate voltage, we charted it against volumetric carrier concentration (Figure S10 in the Supporting Information). These concentrations were derived from gate voltage-dependent Hall effect measurements and adjusted for film thickness. Our experimental findings were paired with theoretical thermopower calculations, based on Boltzmann transport theory and electronic density of states from ab initio simulations (represented by black lines). These calculations also factored in energy-dependent scattering rates in a phenomenological manner. Detailed calculations are available in the Supporting Information. While there is a good alignment between DFT trends and experimental results, DFT tends to undervalue the magnitude of the Seebeck coefficient. This discrepancy might arise from the GGA level of DFT not adequately addressing electron-electron correlation or overlooking polaron formation. Both factors can amplify the effective mass,[34] leading to a higher Seebeck coefficient shown in Figure S10 (Supporting Information) when compared to the calculated value.

To deepen our understanding, we also numerically calculated thermopower using a parabolic band model, parameterized by the effective mass (m^*) and scattering parameter (r), as detailed in the Supporting Information and in reference.[35] By varying the reduced chemical potential, we generated a spectrum of carrier concentrations. We then computed the thermopower across different effective electron masses and scattering parameters, all at a fixed temperature of 300 K. In Figure S10 (Supporting Information), specifically subfigure $r = 2.0$, the nature of the thermoelectric transport remains consistent across doping and gate voltages. There is no notable divergence in experimental trends from those predicted by DFT and the parabolic band model. This consistency indicates that gate-voltage-driven thermoelectric

© 2023 The Authors. Advanced Electronic Materials published by Wiley-VCH GmbH

properties predominantly follow a 3D charge transport mechanism. Significant deviations would have hinted at other transport mechanisms, such as gate voltage-induced conducting layer thinning[21] or the emergence of a 2D electron gas.[22,27,28]

3. Conclusion

In conclusion, we demonstrated the effect of ionic liquid-based gating on the electronic and thermoelectric properties of doped Nb-$SrTiO_3$ thin films grown on LSAT substrates. Ionic gating enhances both carrier concentration and mobility, elevating electronic conductivity without a major impact on the Seebeck coefficient. The strength of the gating effect is significantly influenced by the thickness of films and the intrinsic carrier concentrations. We discovered that reducing the thickness of the film and decreasing the number of inherent charge carriers improves its thermoelectric properties. In our study, we achieved an 18-times increase in power generation efficiency at room temperature for a 14-nanometer-thick film of 4% niobium-doped strontium titanate (Nb-STO) when applying a voltage between plus or minus 3 volts. This research provides additional understanding and innovative approaches for enhancing the thermoelectric properties of thin films that can be adjusted by applying an external voltage.

4. Experimental Section

PLD Targets: Polycrystalline PLD targets of compositions $La_{0.1}Ca_{0.9}MnO_3$ (i.e., 10% La-CMO), $SrTi_{0.94}Nb_{0.06}O_3$ (i.e., 6% Nb-STO), and $SrTi_{0.96}Nb_{0.04}O_3$ (i.e., 4% Nb-STO) were purchased from SurfaceNet. The diameters of these targets are 1 inch and thicknesses are 4 mm.

Thin Film Fabrications: Thin films of Nb-STO were fabricated with pulsed laser deposition (PLD) using 5 × 5 × 0.5 mm^3 single-side polished LSAT-001 substrates with a lattice constant a = 3.870 Å. The substrates were purchased from CrysTec and were cleaned in an acetone bath sonicator followed by washing several times with isopropanol before inserting them in the growth chamber. Film depositions were carried out at 650 °C in a background pressure of 1.24 (±0.2) × 10^{-4} mbar oxygen pressure with a laser fluence of ≈1.15 (±0.03) J.cm^{-2} and a repetition rate of 1 Hz. The distance between the target and the substrate was fixed to 45 mm. No post-annealing treatments were performed in any of the samples presented in this paper.

Structural, Thickness, and Morphological Characterizations: The crystal structure of thin films and their surface morphologies were analyzed by X-ray diffraction (XRD) and atomic force microscopy (AFM) techniques, respectively. The thickness of the patterned Nb-STO Hall bars was measured by analyzing the height profile of topographic-AFM images (see Figure S2 in the Supporting Information).

Device Fabrications: Hall bar patterns of Nb-STO films were prepared by using optical lithography- and wet-etching techniques. The advantage was taken from the fact that La-doped $CaMnO_3$ (La-CMO) films could be etched wet-chemically using XX,[30] while Nb-STO films and the LSAT substrate could not be etched the same way. This selective etching behavior allowed the use of a thin layer of amorphous La-CMO as a hard mask for preparing Hall bars of Nb-STO. The details of the Hall bar fabrications are documented in Figure S1a, in the supporting information.

Electronic Transport and Hall Coefficients Measurements: For electronic transport, Hall coefficients, and thermoelectric power measurements against gate voltages, Hall bars of the Nb-STO films were metalized with patterned Ti/Au electrodes. The process of metallization is shown in Figure S1b, Supporting Information. The details of the device configuration for electronic conductivity and Hall measurements are depicted in Figure S3a–d, Supporting Information. It was assumed that the thicknesses of the Hall bar channels of Nb-STO films do not change during the application of a high electric field and the field is uniform throughout the whole volume of the channel. A fixed current source at 1 × 10^{-6} A was employed between the source and the drain contact for resistance measurements against liquid gating and the leakage current through the gate was <1 nA within $-1.0 \leq V_{LG} \leq +1.0$ V. All measurements were performed in a vacuum to avoid any effect of oxygen. These measurements were performed below the freezing point of the ionic liquid to avoid any thermal fluctuations on the ionic liquid and to achieve a static electric field with low leakage current in the order of pA. Samples were warmed up above the melting point of ionic liquid in order to change gate voltages and then cooled down to 200 K for accurate Hall measurements. Figure S6 in Supporting Information depicts ion-gated Hall measurements for a 17 nm 6% Nb-STO thin film. Hall resistances were linear within ±5 tesla magnetic field. The slope of "Hall resistance versus magnetic field" gives an estimation of the Hall coefficients. The slope increased monotonically when the gate voltage changed from +3.0 to −2.0 V.

Thermoelectric Seebeck Coefficients Measurements: The Seebeck coefficient (S) was defined as the ratio of voltage output (ΔV) pr. unit Kelvin difference in temperature (ΔT) across a material; $S = -\frac{\Delta V}{\Delta T}$. The direction of thermoelectric current or potential was opposite to the charge diffusion from the hot to the cold end, and hence, the negative sign. Therefore, it was necessary to create a gradient of temperatures across the thin films for thermoelectric measurement. A metal line-heater (5 nm Ti/50 nm Au) was fabricated at one side of the LSAT substrate (see Figure 1a,b in the main text and Figure S3e–h in the Supporting Information for details), denoted as I_{Heater}. A set of ΔT was created by applying a range of constant currents to the metal heater, and Seebeck voltages were collected at the same time. For accurate temperature difference measurements at any two points, two 4-point resistors were fabricated, denoted as Th1 and Th2. The electronic resistance of novel metals such as Au was very sensitive to temperatures: it increases linearly with increasing temperature (see Figure 4a in the Supporting Information). From there, the temperature coefficient of resistance was calculated. The variation of resistance was used to estimate the relative change in temperature for both Th1 and Th2 when a range of currents was applied to the heater. These resistors were also used to measure the open circuit Seebeck voltages. The heating effect mainly originates from the Joule´s effect. A real-time Seebeck coefficient measurement is depicted in Figure S4 in the Supporting Information.

Ionic Liquid Gating: 1-ethyl-3-methylimidazolium-bis (trifluoro sulfonyl) amide ionic liquid was used, abbreviated as EMIM-TFSI. It was mixed with poly (styrene-block-methyl methacry-late-block-styrene, abbreviated as PS-PMMA-PS, to form a highly viscous gel. A micro drop of this gel was spread over the Nb-STO Hall bar channel and the gate contact pad ("G").

DFT Calculations and Numerical Analysis: The thermopower was evaluated using BoltzTrap2[31] on the electronic structure calculated using the Vienna Ab initio Simulation Package (VASP).[32] For simplicity, undoped cubic $SrTiO_3$ was used as the model structure, and the lattice parameter was set to 3.896 Å. The generalized gradient approximation (GGA) xc-functional PBE was used.[33] A plane-wave cutoff of 550 eV was set and the self-consistent field solution was converged below 10^{-6} eV. The Brillouin zone was sampled using an 8 × 8 × 8 and 50 × 50 × 50 Γ-centered k-mesh, in the self-consistent charge and band structure calculation, respectively. The Seebeck constant was calculated at 300 K on an interpolated k-grid with a five times higher density using the Fourier interpolation algorithm in BoltzTrap2. The influence of energy-dependent scattering rates was modeled phenomenologically by including a scattering time $\tau = \tau 0\ (E - E_{CBM})(r\text{-}1/2)$, see reference.[34] Note that the prefactor was irrelevant for the Seebeck coefficient and the definition of the scattering parameter, r, differs by ½ from some literature (references).

© 2023 The Authors. Advanced Electronic Materials published by Wiley-VCH GmbH

2199160x, 2024, 3, Downloaded from https://onlinelibrary.wiley.com/doi/10.1002/aelm.202300683 by Danish Technical Knowledge, Wiley Online Library on [21/03/2024]. See the Terms and Conditions (https://onlinelibrary.wiley.com/terms-and-conditions) on Wiley Online Library for rules of use; OA articles are governed by the applicable Creative Commons License

2199160x, 2024, 3, Downloaded from https://onlinelibrary.wiley.com/doi/10.1002/aelm.202300683 by Danish Technical Knowledge, Wiley Online Library on [21/03/2024]. See the Terms and Conditions (https://onlinelibrary.wiley.com/terms-and-conditions) on Wiley Online Library for rules of use; OA articles are governed by the applicable Creative Commons License

Supporting Information

Supporting Information is available from the Wiley Online Library or from the author.

Acknowledgements

N.P. and A.C. acknowledge the support of the European Union's Horizon 2020 research and innovation program under grant agreement number 824072 funded this work. N.P., D.V.C., and C. N. L. also acknowledge the Danish Council for Independent Research Technology and Production Sciences for the DFF- Research Project 3 (grant No 00069B). D.V.C. further acknowledges the support of the Novo Nordisk Foundation NERD Programme: New Exploratory Research and Discovery, Superior Grant NNF21OC0068015.

Conflict of Interest

The authors declare no conflict of interest.

Author Contributions

Conceptualization was done by N.P. and A.C. A.C. who did the thin film fabrication and structural/morphology characterizations. Device fabrication was handled by T. A. A. and A.C. while transport and thermoelectric power measurements were conducted by C.N.L., F.T., J.C.G., and A.C. DFT-based calculations were performed by V.R. N.P. supervised the work, and A.C. and D.V.C. were responsible for data analysis. A.C. and N.P. collaborated on original manuscript writing, and N.P. led funding acquisition. All authors contributed to reviewing and editing the manuscript.

Data Availability Statement

The data that support the findings of this study are available on request from the corresponding author. The data are not publicly available due to privacy or ethical restrictions.

Keywords

and thermoelectric power factor, electric-double-layer transistors, ionic liquid gating, Nb-doped $SrTiO_3$ thin films

Received: October 5, 2023
Revised: November 27, 2023
Published online: December 25, 2023

[1] Q. Zhang, K. Deng, L. Wilkens, H. Reith, K. Nielsch, *Nat. Electron.* **2022**, *5*, 333.
[2] A. Tarancón, *Nat. Electron.* **2019**, *2*, 270.
[3] A. Chatterjee, C. Lobato, H. Zhang, A. Bergne, V. Esposito, S. Yun, A. Insinga, D. Christensen, C. Imbaquingo, R. Bjørk, H. Ahmed, M. Ahmad, C. Ho, M. Madsen, J. Chen, P. Norby, F. Chiabrera, F. Gunkel, Z. Ouyang, N. Pryds, *J. Phys. Energy* **2023**, *5*, 22001.
[4] A. Sarantopoulos, E. Ferreiro-Vila, V. Pardo, C. Magén, M. H. Aguirre, F. Rivadulla, *Phys. Rev. Lett.* **2015**, *115*, 166801.
[5] A. Chatterjee, E. Chavez-Angel, B. Ballesteros, J. Caicedo, J. Padilla-Pantoja, V. Leborán, C. Sotomayor Torres, F. Rivadulla, J. Santiso, *J. Mater Chem A Mater* **2020**, *8*, 19975.
[6] A. Chatterjee, Z. Lan, D. Christensen, F. Bauitti, A. Morata, E. Chavez-Angel, S. Sanna, I. Castelli, Y. Chen, A. Tarancon, N. Pryds, *Phys. Chem. Chem. Phys.* **2022**, *24*, 3741.
[7] B. Jalan, S. Stemmer, *Appl. Phys. Lett.* **2010**, *97*, 042106.
[8] Y. Zhang, B. Feng, H. Hayashi, T. Tohei, I. Tanaka, Y. Ikuhara, H. Ohta, *J. Appl. Phys.* **2017**, *121*, 185102.
[9] Y. Zhang, B. Feng, H. Hayashi, C. Chang, Y.-M. Sheu, I. Tanaka, Y. Ikuhara, H. Ohta, *Nat. Commun.* **2018**, *9*, 2224.
[10] G. Snyder, E. Toberer, *Nat. Mater.* **2008**, *7*, 105.
[11] J. Sootsman, D. Chung, M. Kanatzidis, *Angew. Chemie – Int. Ed.* **2009**, *48*, 8616.
[12] K. Parendo, K. Tan, A. Bhattacharya, M. Eblen-Zayas, N. Staley, A. Goldman, *Phys. Rev. Lett.* **2005**, *94*, 197004.
[13] M. Noroozi, G. Jayakumar, K. Zahmatkesh, J. Lu, L. Hultman, M. Mensi, S. Marcinkevicius, B. Hamawandi, M. Tafti, A. Ergül, Z. Ikonic, M. Toprak, H. Radamson, *ECS J. Solid State Sci. Technol.* **2017**, *6*, Q114.
[14] I. Terasaki, *APL Mater.* **2016**, *4*, 104501.
[15] S. Bisri, S. Shimizu, M. Nakano, Y. Iwasa, *Adv. Mater.* **2017**, *29*, 1607054.
[16] J. Cho, J. Lee, Y. He, B. Kim, T. Lodge, C. Frisbie, *Adv. Mater.* **2008**, *20*, 686.
[17] C. Leighton, *Nat. Mater.* **2019**, *18*, 13.
[18] H. Yuan, H. Shimotani, A. Tsukazaki, A. Ohtomo, M. Kawasaki, Y. Iwasa, *Adv. Funct. Mater.* **2009**, *19*, 1046.
[19] Y. Saito, T. Iizuka, T. Koretsune, R. Arita, S. Shimizu, Y. Iwasa, *Nano Lett.* **2016**, *16*, 4819.
[20] S. Shimizu, M. Bahramy, T. Iizuka, S. Ono, K. Miwa, Y. Tokura, Y. Iwasa, *Proc Natl Acad Sci USA* **2016**, *113*, 6438.
[21] M. Li, T. Graf, T. Schladt, X. Jiang, S. Parkin, *Phys. Rev. Lett.* **2012**, *109*, 196803.
[22] K. Ueno, S. Nakamura, H. Shimotani, A. Ohtomo, N. Kimura, T. Nojima, H. Aoki, Y. Iwasa, M. Kawasaki, *Nat. Mater.* **2008**, *7*, 855.
[23] T. Bretz-Sullivan, A. Goldman, *Appl. Phys. Lett.* **2015**, *107*, 113106.
[24] M. Lee, J. Williams, S. Zhang, C. Frisbie, D. Goldhaber-Gordon, *Phys. Rev. Lett.* **2011**, *107*, 256601.
[25] S. Shimizu, S. Ono, T. Hatano, Y. Iwasa, Y. Tokura, *Phys. Rev. B Condens. Matter Mater. Phys.* **2015**, *92*, 165304.
[26] H. Ohta, T. Mizuno, S. Zheng, T. Kato, Y. Ikuhara, K. Abe, H. Kumomi, K. Nomura, H. Hosono, *Adv. Mater.* **2012**, *24*, 740.
[27] Y. Chen, N. Pryds, J. Kleibeuker, G. Koster, J. Sun, E. Stamate, B. Shen, G. Rijnders, S. Linderoth, *Nano Lett.* **2011**, *11*, 3774.
[28] A. Chatterjee, Z. Lan, D. Christensen, F. Bauitti, A. Morata, E. Chavez-Angel, S. Sanna, I. Castelli, Y. Chen, A. Tarancon, N. Pryds, *Phys. Chem. Chem. Phys.* **2022**, *24*, 3741.
[29] E. Langenberg, E. Ferreiro-Vila, V. Leborán, A. Fumega, V. Pardo, F. Rivadulla, *APL Mater.* **2016**, *4*, 104815.
[30] G. Bridoux, J. Barzola-Quiquia, F. Bern, W. Böhlmann, I. Vrejoiu, M. Ziese, P. Esquinazi, *Nanotechnology* **2012**, *23*, 085302.
[31] G. Madsen, J. Carrete, M. Verstraete, *Comput. Phys. Commun.* **2018**, 140, *231*,.
[32] G. Kresse, J. Furthmüller, *Phys. Rev. B Condens. Matter Mater. Phys.* **1996**, *54*, 11169.
[33] J. Perdew, K. Burke, M. Ernzerhof, *Phys. Rev. Lett.* **1996**, 3865, *77*.
[34] T. Okuda, K. Nakanishi, S. Miyasaka, Y. Tokura, *Phys. Rev. B Condens. Matter Mater. Phys.* **2001**, *63*, 113104.
[35] M. Mirjolet, F. Rivadulla, P. Marsik, V. Borisov, R. Valentí, J. Fontcuberta, *Adv. Sci.* **2021**, *8*, 202004207.
[36] H. Ni, M. Zheng, L. Chen, W. Huang, Y. Qi, J. Zeng, Z. Tang, H. Lu, J. Gao, *Appl. Phys. Lett.* **2017**, *110*, 213503.

© 2023 The Authors. Advanced Electronic Materials published by Wiley-VCH GmbH